AAAS
Research
Volume 2022, Article ID 9767651, 11 pages
https://doi.org/10.34133/2022/9767651

Research Article

Realization of Oriented and Nanoporous Bismuth Chalcogenide Layers via Topochemical Heteroepitaxy for Flexible Gas Sensors

Zhiwei Wang,[1,2] Jie Dai,[1] Jian Wang,[1] Xinzhe Li,[1] Chengjie Pei,[1] Yanlei Liu,[1] Jiaxu Yan,[1] Lin Wang,[1] Shaozhou Li,[3] Hai Li,[1] Xiaoshan Wang,[2] Xiao Huang,[1] and Wei Huang[1,2,3]

[1]*Institute of Advanced Materials (IAM), Nanjing Tech University (NanjingTech), 30 South Puzhu Road, Nanjing 211816, China*
[2]*Frontiers Science Center for Flexible Electronics, Xi'an Institute of Flexible Electronics (IFE) and Xi'an Institute of Biomedical Materials & Engineering, Northwestern Polytechnical University, 127 West Youyi Road, Xi'an 710072, China*
[3]*Key Laboratory for Organic Electronic & Information Displays (KLOEID) and Jiangsu Key Laboratory for Biosensors, Institute of Advanced Materials (IAM), Nanjing University of Posts and Telecommunications, 9 Wenyuan Road, Nanjing 210023, China*

Correspondence should be addressed to Xiaoshan Wang; iamxswang@nwpu.edu.cn, Xiao Huang; iamxhuang@njtech.edu.cn, and Wei Huang; iamwhuang@nwpu.edu.cn

Received 15 March 2022; Accepted 24 May 2022; Published 24 June 2022

Most van der Waals two-dimensional (2D) materials without surface dangling bonds show limited surface activities except for their edge sites. Ultrathin Bi_2Se_3, a topological insulator that behaves metal-like under ambient conditions, has been overlooked on its surface activities. Herein, through a topochemical conversion process, ultrathin nanoporous Bi_2Se_3 layers were epitaxially deposited on BiOCl nanosheets with strong electronic coupling, leading to hybrid electronic states with further bandgap narrowing. Such oriented nanoporous Bi_2Se_3 layers possessed largely exposed active edge sites, along with improved surface roughness and film forming ability even on inkjet-printed flexible electrodes. Superior room-temperature NO_2 sensing performance was achieved compared to other 2D materials under bent conditions. Our work demonstrates that creating nanoscale features in 2D materials through topochemical heteroepitaxy is promising to achieve both favorable electronic properties and surface activity toward practical applications.

1. Introduction

Bismuth-based two-dimensional (2D) layered materials, such as bismuth chalcogenides [1, 2], bismuth oxyhalides [3, 4], and bismuth halides [5, 6], are emerging eco-friendly functional materials that find wide applications in electronics, optoelectronics and energy conversion, and storage devices [7–9]. Bi_2Se_3 possesses excellent electrical conductivity even under a high density of defects and dislocations, since its surface states are protected from scattering [10–12]. Nanostructures of Bi_2Se_3 have recently shown potential in photothermal cancer therapy [13], optical switching [14], and thermoelectric devices [15]. In addition, they have also been combined with other nanostructures, such as graphene [16], ZnO [17], and $CsPbBr_3$ [18], for enhanced photoabsorption, stimulated surface-plasmon polaritons, and enhanced exciton transfer efficiency, respectively. However, despite their outstanding electronic and optoelectronic properties, the surface activities of Bi_2Se_3 seem to be overlooked and less explored.

Bismuth oxyhalides (BiOX, where X = Cl, Br, and I) are particularly promising in photocatalytic energy conversion and environmental remediation [19–22]. BiOCl is perhaps one of the most investigated bismuth oxyhalides because of its low toxicity and high stability [23, 24]. However, its relatively large bandgap (typically ~3.2 eV) has limited its electronic and optoelectronic applications [22]. To date, many strategies have been developed to improve its properties, including morphology control [25], tuning of exposed crystal facets [21], and surface modification [26]. The construction of heterostructures, by considering band level alignment, has been proven effective in modifying its electronic properties, with examples including $BiOCl/TiO_2$ [27], $BiOCl/WO_3$ [28], $BiOCl/ZnSn(OH)_6$ [29], and BiOCl/BiOI [30]. Epitaxial heterostructures are important

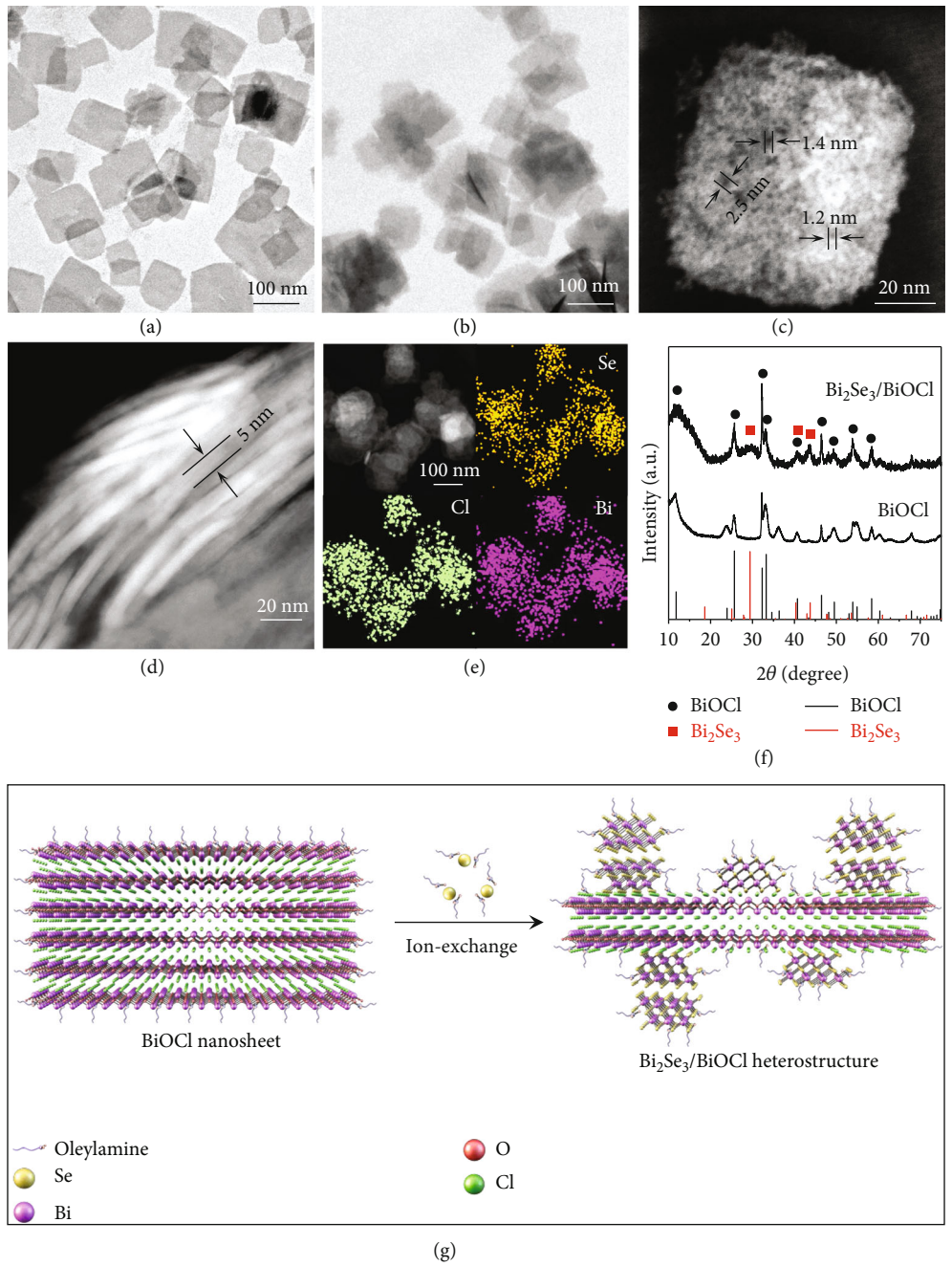

Figure 1: TEM images of (a) BiOCl nanosheets and (b) Bi_2Se_3/BiOCl heterostructures. (c) STEM image of a Bi_2Se_3/BiOCl heterostructure, revealing a nanoporous Bi_2Se_3 layer with a pore size of 1-3 nm. (d) Side-view STEM image of Bi_2Se_3/BiOCl heterostructures. (e) STEM image and EDX mapping of Bi_2Se_3/BiOCl heterostructures. (f) XRD patterns of BiOCl nanosheets and Bi_2Se_3/BiOCl heterostructures. (g) Schematic illustration of the formation process of the Bi_2Se_3/BiOCl heterostructure.

with controllable overlayer orientation and coherent heterointerfaces [31]. Till now, solution-phased methods such as the coupling reaction [32] and self-assembly process [33] have been developed for preparing epitaxial heterostructures. However, the solution phase synthesis of BiOCl-based epitaxial heterostructures has been rarely explored.

Gas sensors are needed in many applications, including medical diagnosis [34], environmental monitoring [35], food quality assessment [36], and military applications [37]. Ultrathin 2D materials as well as their heterostructures have been applied to gas sensing due to large specific surface areas and tunable electronic and mechanical properties [38–41]. Many 2D materials, especially van der Waals 2D materials without surface dangling bonds, show higher activities at edges than at basal surfaces. However, maximizing edge exposure and increasing the edge/basal surface ratio remain great challenges.

In this study, we report the epitaxial growth of nanoporous Bi_2Se_3 with largely exposed edge sites on BiOCl nanosheets via an anion exchange-induced topochemical

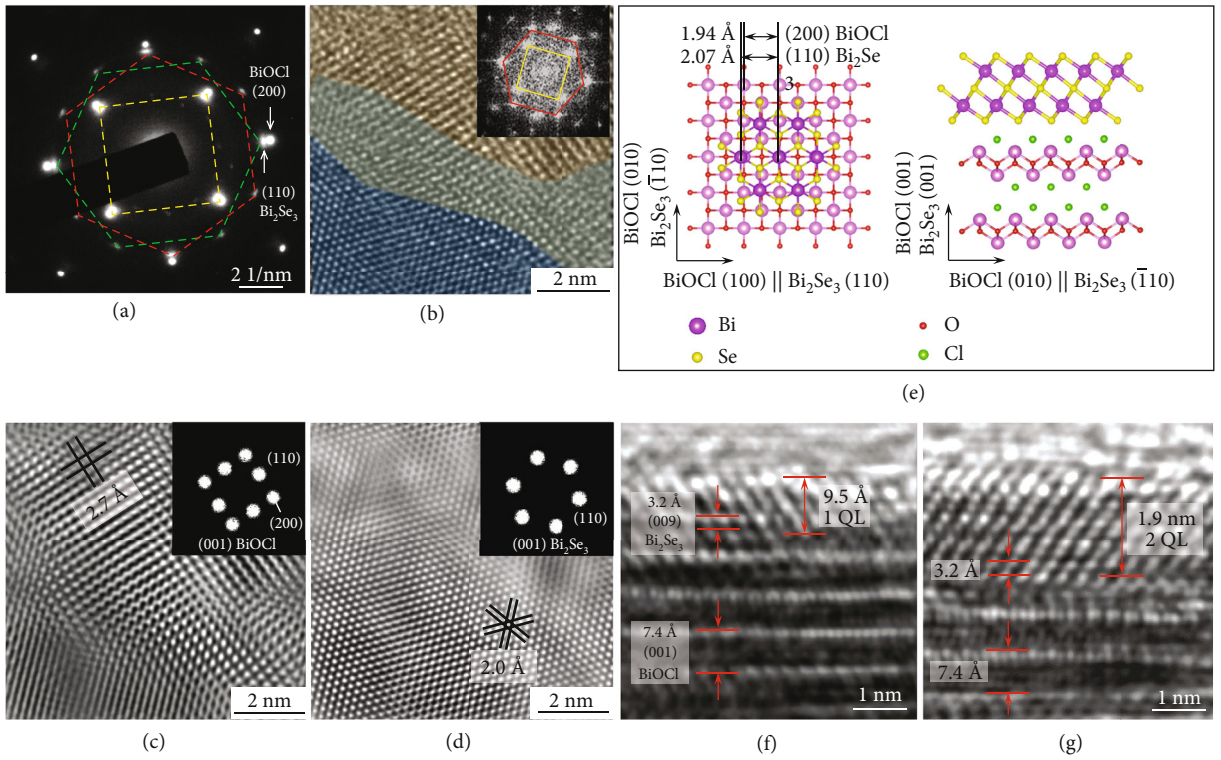

FIGURE 2: (a) SAED pattern of a Bi_2Se_3/BiOCl heterostructure. The pattern for BiOCl with a fourfold symmetry is indicated by a yellow square; two patterns for Bi_2Se_3 with a sixfold symmetry are indicated by red and green hexagons. (b) HRTEM image of an area with overlapping lattices of BiOCl and Bi_2Se_3. Inset: the corresponding FFT diffraction pattern. (c) BiOCl [001]-zone and (d) Bi_2Se_3 [001]-zone lattice patterns generated by performing inverse-FFT of the spots forming the red hexagon and the yellow square in (b), respectively. Insets in (c and d): the selected spots. (e) Schematic top-view and side-view models indicating the BiOCl (001) || Bi_2Se_3 (001) and BiOCl [100] || Bi_2Se_3 [110] epitaxial relationship. Side-view HRTEM images of typical Bi_2Se_3/BiOCl heterostructures with (f) 1 QL and (g) 2 QLs Bi_2Se_3 grown on a BiOCl nanosheet.

conversion process. Bi_2Se_3/BiOCl epitaxial heterostructures were used to detect NO_2 gas and demonstrated good sensing performance even on printed flexible electrodes under bent conditions. This can be attributed to the strong electronic coupling across the Bi_2Se_3/BiOCl heterointerface, the enhanced surface activity of Bi_2Se_3, and the improved film forming ability with sub-2 nm surface features.

2. Results and Discussion

A solvothermal method was used to synthesize BiOCl nanosheets by following a previous report [22]. A solution of Se dissolved in oleylamine (OLA) and dodecanethiol (DDT) was then hot-injected into the BiOCl nanosheet solution and heated to induce the growth of Bi_2Se_3 on BiOCl.

The BiOCl nanosheets and Bi_2Se_3/BiOCl heterostructures were characterized with transmission electron microscopy (TEM), energy dispersive X-ray spectroscopy (EDX), X-ray diffraction (XRD), and X-ray photoelectron spectroscopy (XPS), as shown in Figure 1 and Figure S1. The original BiOCl nanosheets were square-shaped with an average edge length of ~90 nm (Figure 1(a)) and thickness of 5-8 nm (Figure S1a). After being hybridized with Bi_2Se_3, the square shape of the BiOCl nanosheets remained, and their surfaces became fluffier (Figure 1(b)). The dark-field scanning transmission electron microscopy (STEM) images reveal that there are pores on the surface of the nanosheets, some of which are less than 2 nm in size (Figure 1(c) and Figure S1b, c), which was further proved by the pore size distribution curve extracted from the N_2 adsorption-desorption isotherm curve (Figure S2). The thickness of the hybrid nanosheets, as estimated from their side-view STEM image, was ~5 nm (Figure 1(d)). Their EDX mapping analysis confirms the presence of Se, Cl, and Bi elements (Figure 1(e)), and the XRD pattern (Figure 1(f)) reveals peaks from both BiOCl (JCPDS no. 06-0249, space group $P4/nmm$, $a = 0.3891$ nm and $c = 0.7369$ nm) and Bi_2Se_3 (JCPDS no. 33-0214, space group $R\bar{3}m$, $a = 0.4139$ nm, and $c = 2.8636$ nm) [22, 42]. Their XPS Bi 4f spectrum shows two doublets for Bi^{3+} at 157.5/162.8 eV and 158.5/163.8 eV attributed to the different binding states of Bi in Bi_2Se_3 and BiOCl, respectively (Figure S3) [43, 44]. From the convoluted XPS peak areas, the Bi_2Se_3: BiOCl molar ratio can be estimated as 3 : 5 [45]. The formation of the Bi_2Se_3/BiOCl heterostructures is likely a result of an in situ ion-exchange reaction, as schematically shown in Figure 1(g). During this process, the Se powder dissolved in OLA and DDT was reduced to Se^{2-} and complexed with OLA based on Equation (1) [46]. The surface layer of BiOCl might

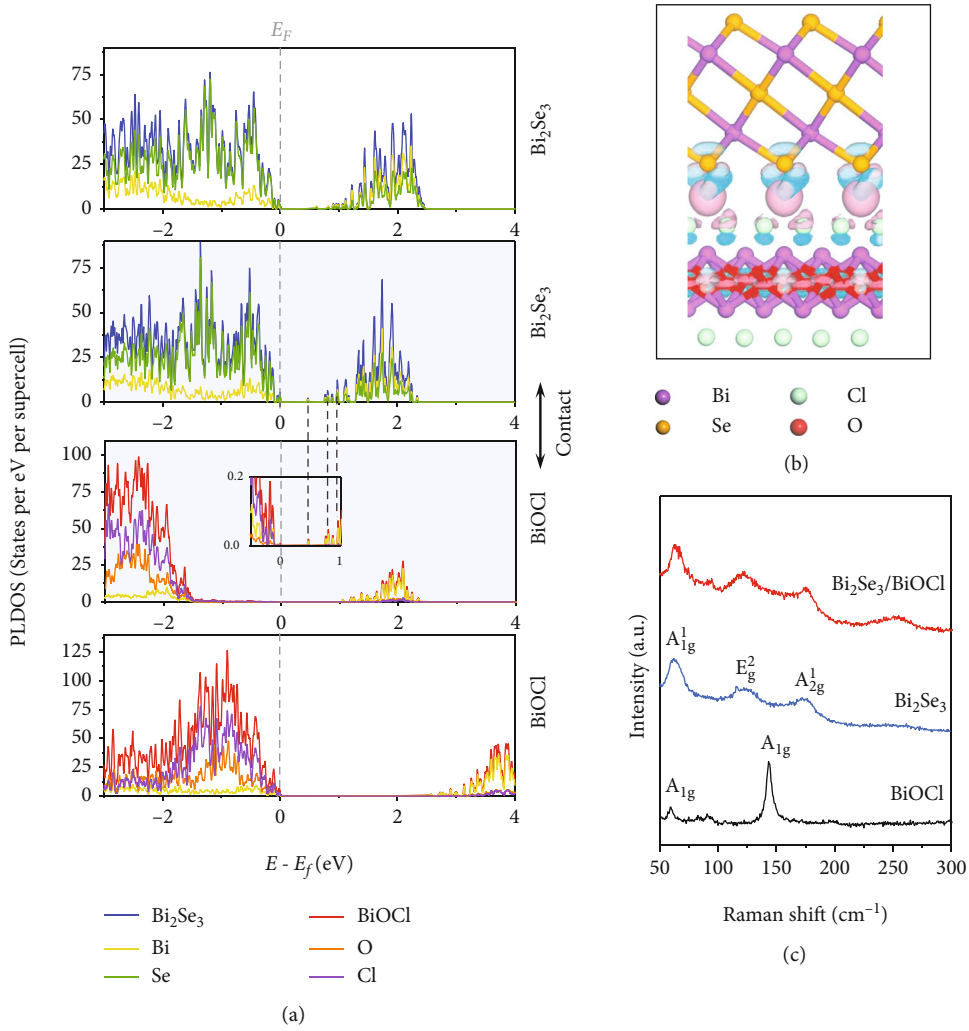

FIGURE 3: (a) Calculated PLDOS of Bi_2Se_3 (the top 1st panel) and BiOCl (bottom panel) before and after (the 2nd and 3rd panels) contact. (b) Calculated structure model of the Bi_2Se_3-BiOCl interface superimposed with the charge density difference (cyan: positive; pink: negative). (c) Raman spectra of BiOCl, Bi_2Se_3, and Bi_2Se_3/BiOCl heterostructures.

undergo an ion exchange reaction with the surrounding Se^{2-} to produce Bi_2Se_3 (Equation (2)). This proposed in situ ion exchange process is also consistent with the observation that the Bi_2Se_3/BiOCl hybrid nanosheets did not become thicker than the original BiOCl nanosheets.

$$2\mathrm{OLA} + \mathrm{Se} + 2\mathrm{HSC_{15}H_{25}} \longrightarrow (\mathrm{OLA})_2\mathrm{Se} + \mathrm{H_{25}C_{12}S_2C_{12}H_{25}}, \quad (1)$$

$$2\mathrm{BiOCl} + 3(\mathrm{OLA})_2\mathrm{Se} \longrightarrow \mathrm{Bi_2Se_3} + 2(\mathrm{OLA})_2\mathrm{O} + 2(\mathrm{OLA})\mathrm{Cl}. \quad (2)$$

The microstructure of the obtained heterostructure was investigated with selected area electron diffraction (SAED) and high-resolution TEM (HRTEM), as shown in Figure 2. The SAED pattern shows three sets of patterns (Figure 2(a)). One has a fourfold symmetry (indicated by the yellow square) corresponding to BiOCl, and the other two have a sixfold symmetry (indicated by the red and green hexagons) corresponding to Bi_2Se_3. The presence of two hexagonal patterns suggests that the Bi_2Se_3 overlayer has two equivalent alignment directions with a relative rotation angle of 90°. In other words, the (110) planes of Bi_2Se_3 can be aligned with either the (200) or (020) planes of BiOCl, establishing an epitaxial relationship of BiOCl (001) || Bi_2Se_3 (001) and BiOCl [100] || Bi_2Se_3 [110]. In the HRTEM image in Figure 2(b), an overlap of lattice patterns of Bi_2Se_3 and BiOCl can be observed, and its fast Fourier transformation-(FFT-) generated diffraction pattern shows two sets of spots. By selecting the respective set of spots, the BiOCl [001]-zone and the Bi_2Se_3 [001]-zone lattice patterns were regenerated and are shown in Figures 2(c) and 2(d), respectively, further confirming the epitaxial relationship shown in Figure 2(e). The side-view HRTEM images of typical hybrid nanosheets show lattice spacings of 0.32 and 0.74 nm, attributable to the Bi_2Se_3 (009) and BiOCl (001) planes, respectively (Figures 2(f) and 2(g)). It can also be seen that the surface

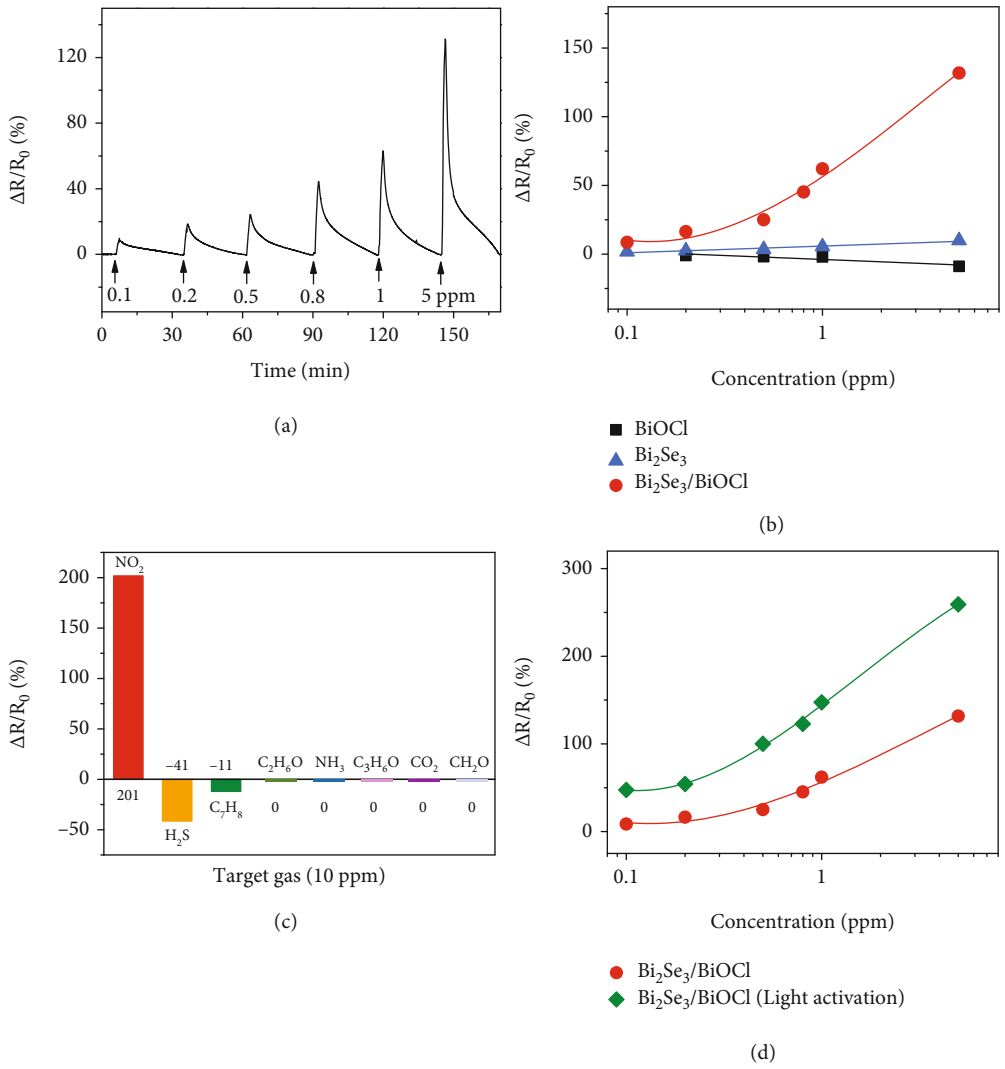

FIGURE 4: (a) Dynamic response-recovery curve of the sensor fabricated from Bi_2Se_3/BiOCl heterostructures in response to NO_2 gas with increasing gas concentration at room temperature. (b) Sensing response vs. NO_2 concentration for BiOCl-, Bi_2Se_3-, and Bi_2Se_3/BiOCl-based sensors. (c) Response of Bi_2Se_3/BiOCl heterostructures upon exposure to 10 ppm NO_2, H_2S, C_7H_8, C_2H_5OH, NH_3, $(CH_3)_2CO$, CO_2, and HCHO at room temperature. (d) Sensing response vs. NO_2 concentration for Bi_2Se_3/BiOCl-based sensor with and without a 365 nm light irradiation (8.31 μW).

deposited Bi_2Se_3 layer contains one quintuple layer (QL) or two QLs.

The energy levels of BiOCl and Bi_2Se_3 (Figure S4, 5) were determined with UV-vis absorption spectra (Figure S6) and UV photoelectron spectroscopy (UPS, Figure S7). The results show that while Bi_2Se_3 shows n-type semiconducting behavior, BiOCl is a p-type semiconductor, consistent with previous reports [47, 48]. The electronic properties of the heterostructure were further studied with first-principle calculations based on density functional theory (DFT). A supercell based on 2 L Bi_2Se_3 and 2 L BiOCl was built, its geometric structure was optimized, and the projected local density of states (PLDOS) was calculated (Figures 3(a) and 3(b) and Figure S8). The Fermi level of BiOCl shifts closer to its conduction band edge after forming a heterojunction with Bi_2Se_3 (Figure 3(a)), suggesting electron transfer from Bi_2Se_3 to BiOCl across the interface. A zoomed-in PLDOS plot for BiOCl in the heterostructure (inset in the 3rd panel in Figure 3(a)) shows new states that follow the projected states of Bi_2Se_3 (2nd panel in Figure 3(a)), resulting in bandgap narrowing at the interface. The charge transfer across the interface can also be seen from the mapping of the charge density difference, in which electron deficient regions are observed on the Bi_2Se_3 side and electron rich regions appear toward the BiOCl side (Figure 3(b)). Such charge transfer across the interface and the change of the band structure of BiOCl were further demonstrated by the absence of the characteristic Raman peak for BiOCl (A_{1g} mode at 144 cm^{-1}) in the Bi_2Se_3/BiOCl heterostructure (Figure 3(c)) [49, 50].

The large specific surface area enabled by the formation of a nanoporous surface layer and the additional charge transfer channels enabled by the new electronic states upon

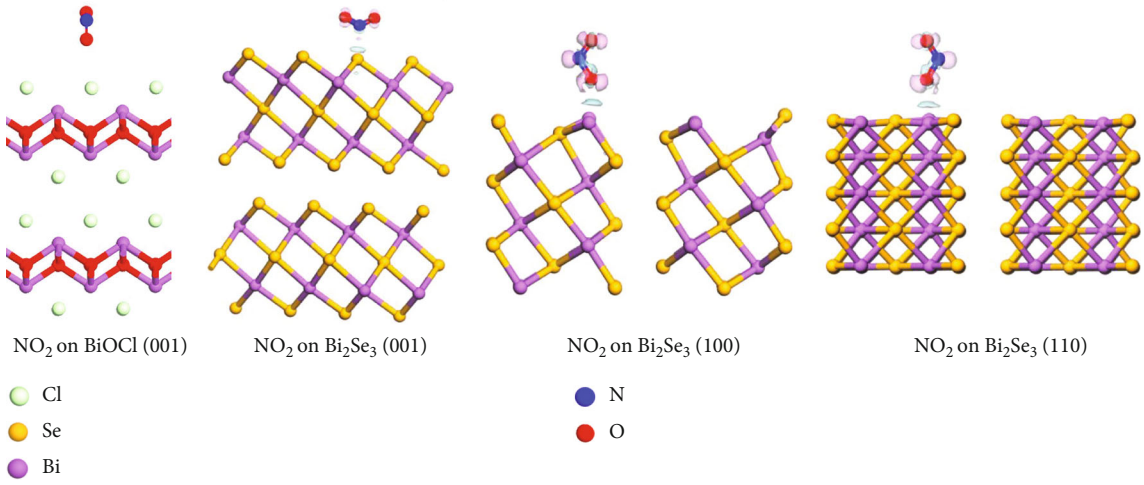

(a)

	Adsorption energy (eV)	Charge transferred (e)
BiOCl (001)	−0.005	−0.04
Bi_2Se_3 (001)	−0.006	−0.15
Bi_2Se_3 (100)	−1.18	−0.55
Bi_2Se_3 (110)	−0.73	−0.53

(b)

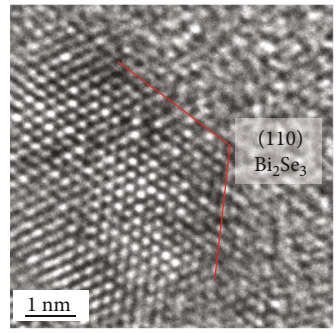

(c)

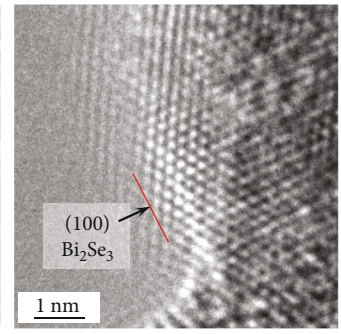

(d)

Figure 5: (a) Calculated structural models of NO_2 molecules absorbed on the BiOCl (001), Bi_2Se_3 (001), (100), and (110) surfaces. (b) Calculated adsorption energy (eV) and electron transferred (e) toward NO_2 on different sensing surfaces. HRTEM images showing the (c) (110) edge plane and (d) (100) edge plane of Bi_2Se_3.

heterojunction formation suggest that our epitaxial heterostructures are promising for sensing applications. As a proof-of-concept demonstration, the NO_2 gas sensing properties of BiOCl nanosheets, Bi_2Se_3 nanosheets, and Bi_2Se_3/BiOCl heterostructures were studied at room temperature (Figures 4(a) and 4(b) and Figure S9). To preclude the influence of the baseline shift, baseline correction was implemented for the sensing responses (Figure S10) [51–53]. Upon exposure to NO_2 (an oxidizing gas), the BiOCl film and Bi_2Se_3 film showed decreased and increased resistance, respectively, consistent with their *p*-type and *n*-type semiconducting properties [54–57]. However, their sensitivities are poor (e.g., 1.8% response at 1 ppm for BiOCl and 5.4% response at 1 ppm for Bi_2Se_3). The sensor based on Bi_2Se_3/BiOCl, which also showed an increased resistance upon NO_2 exposure, exhibited ~35 and ~12 times higher responses than BiOCl and Bi_2Se_3 at 1 ppm, respectively (Figures 4(a) and 4(b)). In addition, the porous structure of the surface layer of the heterostructure resulted in a large specific surface area, which allowed more gas molecules to interact with the sensing material, but might cause a problem of slow gas desorption [58, 59]. This was also reflected in the slower recovery times than response times (Figure S11). The sensor was also capable of providing a 9.4% response at 100 ppb, along with good reproducibility (Figure S12). Its good selectivity toward NO_2 was proven by exposing it to different gases at 10 ppm, including NO_2, H_2S, C_7H_8, C_2H_5OH, NH_3, $(CH_3)_2CO$, CO_2, and HCHO, at room temperature (Figure 4(c)). The sensing response of Bi_2Se_3/BiOCl could be further improved by light irradiation (Figure 4(d) and Figure S13). This is consistent with the charge transfer and carrier modulation-based sensing mechanism of this type of chemiresistive sensors.

The enhanced sensing performance of the Bi_2Se_3/BiOCl gas sensor at room temperature can be explained from the following aspects. First, since the sensing mechanism of our sensors is mainly based on charge transfer [60], DFT calculations were performed to shed light on how effective the NO_2 adsorption can take away electrons from the heterostructures (Figure 5(a)). The adsorption energies of NO_2 on the (110), (100), and (001) planes of Bi_2Se_3 were calculated to be -0.73 eV, -1.18 eV, and -0.006 eV, respectively, which are more negative than that on BiOCl (001) (-0.005 eV), indicating the higher affinity of NO_2 toward Bi_2Se_3. Note that the edges of Bi_2Se_3 layers, i.e., the (110) and (100) facets are particularly more effective in NO_2 adsorption and charge transfer compared to those on the (001) basal plane (Figure 5(b)). Indeed, the nanoporous

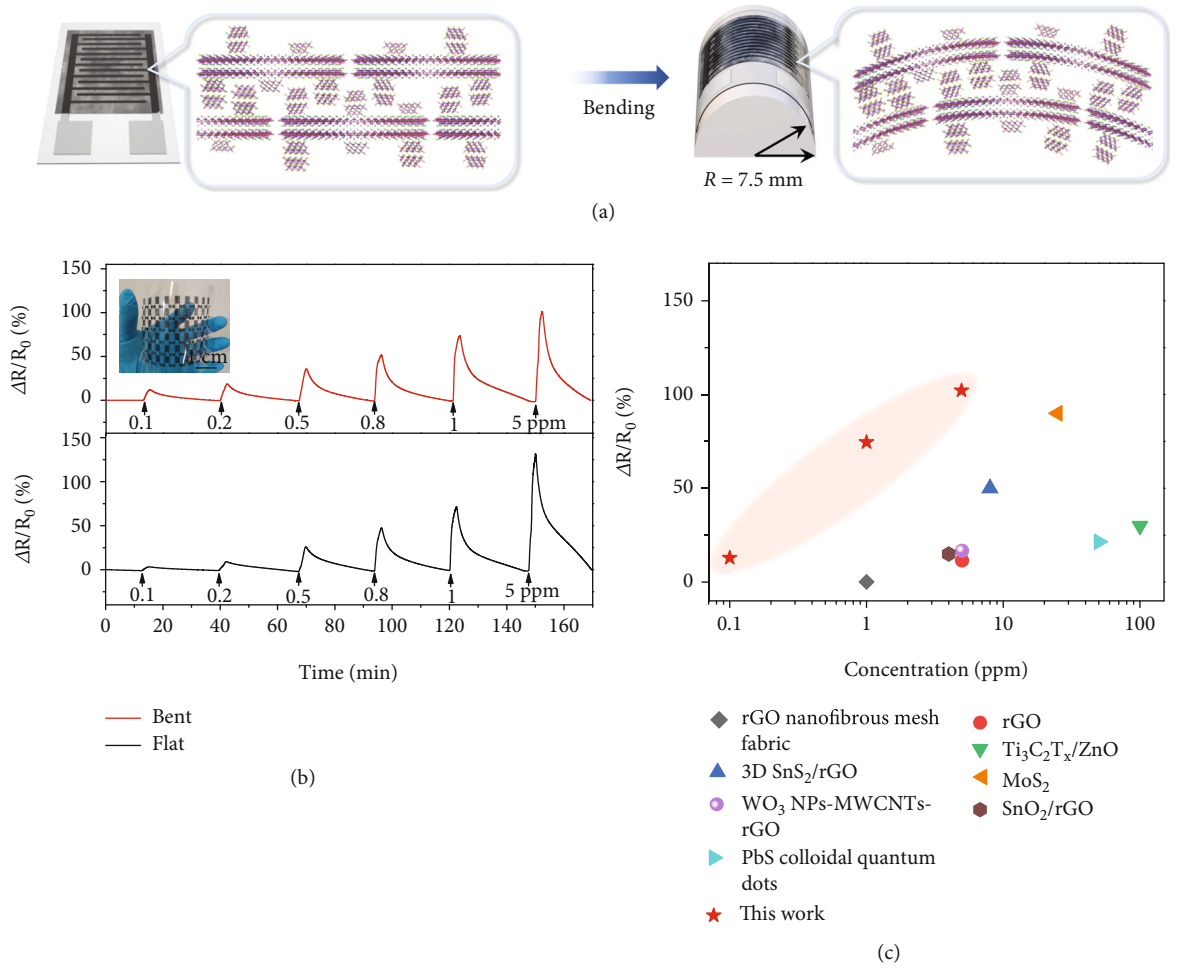

FIGURE 6: (a) Schematic diagram of the Bi_2Se_3/BiOCl heterostructures on flat and bent substrates. (b) Responses of Bi_2Se_3/BiOCl-based sensors under flat and bent states at various NO_2 concentrations. Inset: a photograph of the printed electrode array. (c) Comparison of the sensing performance between our flexible gas sensor and other 2D material-based flexible sensors under bending conditions.

Bi_2Se_3 layer epitaxially deposited on BiOCl was (001)-oriented, showing exposed (110) and (100) facets (Figures 5(c) and 5(d)), thus, favoring NO_2 adsorption and electron transfer.

The improved sensing ability can also be attributed, in part, to the formation of a *p-n* junction at the epitaxial interface between BiOCl and Bi_2Se_3 (Figure S14), where the interdiffusion of electrons and holes across the interface created a charge depletion region along with a built-in potential barrier [61–64]. The height of the energy barrier was mainly determined by the hole concentration in BiOCl because of the much wider bandgap of BiOCl than that of Bi_2Se_3 [65, 66]. Exposure of Bi_2Se_3/BiOCl to NO_2 gas increased the hole concentration in BiOCl, leading to a wider depletion region and thus a higher energy barrier. Because the conductance of the sensing material changes exponentially with the energy barrier at the heterojunction [67, 68], a much improved gas sensing response can be obtained. A higher carrier concentration in BiOCl could be achieved by light irradiation, as shown in Figure 4(d), where the sensing response of the Bi_2Se_3/BiOCl sensor doubled under 365 nm light excitation (8.31 μW).

Moreover, the Bi_2Se_3/BiOCl heterostructure-based sensor showed a faster response time than both Bi_2Se_3 and BiOCl sensors (Figure S11). This can be attributed to the newly generated hybrid electronic states upon formation of epitaxial interface, as shown in the calculated PLDOS in Figure 3(a). These hybrid states could provide additional and faster channels to lose electrons to NO_2, and therefore, a shorter response time was observed for the Bi_2Se_3/BiOCl-based sensing material.

Last, flexible gas sensors based on Bi_2Se_3/BiOCl heterostructures were fabricated by depositing them on a plastic substrate with inkjet-printed interdigitated electrodes (Figure 6). It is worth mentioning that flexible electrodes fabricated with facile printing techniques such as inkjet printing suffer from poor resolution and large gaps between electrodes. This can cause reduced device performance compared to using electrodes fabricated by standard lithography techniques. The growth of the nanoporous Bi_2Se_3 layer on the BiOCl nanosheet increased the surface roughness and might help enhance the interlocking between the stacked hybrid nanosheets (Figure 6(a)). This ensured the formation of a continuous sensing film across the printed electrodes

with a large gap of ~200 μm (Figure S15), even though the average lateral size of the Bi_2Se_3/BiOCl nanosheets was less than 100 nm (Figure 1(b)). In sharp contrast, pristine BiOCl nanosheets deposited on inkjet-printed electrodes failed to form conductive films (Figure S16). The response of the flexible gas sensor under bent conditions (bending radius: 7.5 mm) showed a slightly enhanced response at sub-ppm levels compared to that under flat conditions, with a calculated limit of detection down to 1.6 ppb (Figure 6(b) and Figure S17), outperforming previously reported flexible sensors based on 2D materials under bent conditions (Figure 6(c) and Table S1) [69–75]. In addition, the bending radius also influenced the sensing performance. A further reduced bending radius to 5 mm could induce more exposed active edge sites and thus higher responses at sub-ppm levels (Figure S18). Last, the mechanical durability of our flexible sensors was tested by repeatedly bending a sensor for 100 times. The sensor maintained approximately 95% of its original response toward 5 ppm NO_2 (Figure S19).

3. Conclusion

In this work, we demonstrated the in situ topochemical conversion of layered materials, which is capable of maximizing the active edge sites of the deposited overlayers and the formation of coherent heterointerfaces. Using Bi_2Se_3/BiOCl as a demonstration, onto BiOCl (001) basal surfaces with fourfold symmetry, hexagonal Bi_2Se_3 (001) layers were epitaxially deposited with largely exposed (100) and (110) edge sites. Compared to BiOCl or Bi_2Se_3 alone, the Bi_2Se_3/BiOCl heterostructure showed a much enhanced sensing response toward NO_2 gas. According to the theoretical calculation results, the Bi_2Se_3 edge surfaces are generally more active than the basal surfaces of Bi_2Se_3 and BiOCl in NO_2 adsorption and charge transfer. Flexible gas sensors based on Bi_2Se_3/BiOCl heterostructures possess good sensing properties with a limit of detection down to 1.6 ppb at room temperature, demonstrating their potential for wearable and portable devices in the future. Our strategy of generating nanopores in van der Waals layered materials via topochemical heteroepitaxy will provide more opportunities to tailor both their electronic and chemical properties.

Data Availability

The data used to support the findings of this study are available from the corresponding authors upon request.

Conflicts of Interest

The authors declare no conflicts of interest.

Authors' Contributions

This study was conceived and designed by W. Huang, X. Huang, and X. Wang. Z. Wang and J. Dai synthesized the samples, conducted the characterization, and analyzed the results. J. Wang, X. Li, and C. Pei conducted flexible gas sensor fabrication and Raman characterization, respectively. Y. Liu, J. Yan, L. Wang, S. Li, and H. Li cowrote the manuscript with input from all authors. Z. Wang and J. Dai contributed equally to this work.

Acknowledgments

This work was supported by the National Key Basic Research Program of China (grant no.: 2021YFB3200302), the National Natural Science Foundation of China (grant nos.: 51832001 and 52102114), the Fundamental Research Funds for the Central Universities of China, the Joint Research Funds of Department of Science & Technology of Shaanxi Province and Northwestern Polytechnical University (grant nos.: 2020GXLH-Z-026 and 2020GXLH-Z-027), the China Postdoctoral Science Foundation (grant nos.: 2021M692618 and 2021M702657), and the Natural Science Foundation of Shaanxi Province (2021JQ-112).

Supplementary Materials

The detailed experimental methods on materials, synthesis of BiOCl nanosheets, synthesis of Bi2Se3 nanosheets, synthesis of Bi2Se3/BiOCl nanosheets, fabrication of chemiresistive sensors and gas sensing tests, fabrication of flexible sensors, characterization, and computational details, Figures S1-S19 and Table S1 are incorporated in the supplementary material. *(Supplementary Materials)*

References

[1] Q. Jin, S. Jiang, Y. Zhao et al., "Flexible layer-structured Bi_2Te_3 thermoelectric on a carbon nanotube scaffold," *Nature Materials*, vol. 18, no. 1, pp. 62–68, 2019.

[2] J. Yao, K. J. Koski, W. Luo et al., "Optical transmission enhacement through chemically tuned two-dimensional bismuth chalcogenide nanoplates," *Nature Communications*, vol. 5, no. 1, article 5670, 2014.

[3] Y. Shi, J. Li, C. Mao et al., "Van Der Waals gap-rich BiOCl atomic layers realizing efficient, pure-water CO_2-to-CO photocatalysis," *Nature Communications*, vol. 12, no. 1, article 5923, 2021.

[4] M. Li, S. Yu, H. Huang et al., "Unprecedented eighteen-faceted BiOCl with a ternary facet junction boosting cascade charge flow and photo-redox," *Angewandte Chemie International Edition*, vol. 58, no. 28, pp. 9517–9521, 2019.

[5] Y. Dai, C. Poidevin, C. Ochoa-Hernández, A. A. Auer, and H. Tüysüz, "A supported bismuth halide perovskite photocatalyst for selective aliphatic and aromatic C–H bond activation," *Angewandte Chemie International Edition*, vol. 59, no. 14, pp. 5788–5796, 2020.

[6] L. Yao, Z. Zeng, C. Cai et al., "Strong second- and third-harmonic generation in 1D chiral hybrid bismuth halides," *Journal of the American Chemical Society*, vol. 143, no. 39, pp. 16095–16104, 2021.

[7] Y. Chen, C. Tan, H. Zhang, and L. Wang, "Two-dimensional graphene analogues for biomedical applications," *Chemical Society Reviews*, vol. 44, no. 9, pp. 2681–2701, 2015.

[8] X. Zhang, H. Cheng, and H. Zhang, "Recent progress in the preparation, assembly, transformation, and applications of

layer-structured nanodisks beyond graphene," *Advanced Materials*, vol. 29, no. 35, article 1701704, 2017.

[9] W. Zhai, T. Xiong, Z. He et al., "Nanodots derived from layered materials: synthesis and applications," *Advanced Materials*, vol. 33, no. 46, article 2006661, 2021.

[10] H. Zhang, X. Zhang, C. Liu, S. Lee, and J. Jie, "High-responsivity, high-detectivity, ultrafast topological insulator Bi_2Se_3/silicon heterostructure broadband photodetectors," *ACS Nano*, vol. 10, no. 5, pp. 5113–5122, 2016.

[11] G. Zhang, H. Qin, J. Teng et al., "Quintuple-layer epitaxy of thin films of topological insulator Bi_2Se_3," *Applied Physics Letters*, vol. 95, no. 5, article 053114, 2009.

[12] H. Peng, K. Lai, D. Kong et al., "Aharonov-Bohm interference in topological insulator nanoribbons," *Nature Materials*, vol. 9, no. 3, pp. 225–229, 2010.

[13] H. Xie, Z. Li, Z. Sun et al., "Metabolizable ultrathin Bi_2Se_3 nanosheets in imaging-guided photothermal therapy," *Small*, vol. 12, no. 30, pp. 4136–4145, 2016.

[14] Y. Hu, M. Tong, X. A. Cheng et al., "Bi_2Se_3-functionalized metasurfaces for ultrafast all-optical switching and efficient modulation of terahertz waves," *ACS Photonics*, vol. 8, no. 3, pp. 771–780, 2021.

[15] Y. Xiong, G. Zhou, N.-C. Lai et al., "Chemically switchable n-type and p-type conduction in bismuth selenide nanoribbons for thermoelectric energy harvesting," *ACS Nano*, vol. 15, no. 2, pp. 2791–2799, 2021.

[16] J. Kim, S. Park, H. Jang et al., "Highly sensitive, gate-tunable, room-temperature mid-infrared photodetection based on graphene–Bi2Se3 heterostructure," *ACS Photonics*, vol. 4, no. 3, pp. 482–488, 2017.

[17] M. Baitimirova, J. Andzane, R. Viter et al., "Improved crystalline structure and enhanced photoluminescence of ZnO nanolayers in Bi_2Se_3/ZnO heterostructures," *The Journal of Physical Chemistry C*, vol. 123, no. 51, pp. 31156–31166, 2019.

[18] Y. Tang, T. Jiang, T. Zhou et al., "Ultrafast exciton transfer in perovskite CsPbBr3quantum dots and topological insulator Bi2Se3film heterostructure," *Nanotechnology*, vol. 30, no. 32, article 325702, 2019.

[19] J. Di, J. Xia, H. Li, S. Guo, and S. Dai, "Bismuth oxyhalide layered materials for energy and environmental applications," *Nano Energy*, vol. 41, pp. 172–192, 2017.

[20] S. Wang, X. Hai, X. Ding et al., "Light-switchable oxygen vacancies in ultrafine Bi_5O_7Br nanotubes for boosting solar-driven nitrogen fixation in pure water," *Advanced Materials*, vol. 29, no. 31, article 1701774, 2017.

[21] J. Jiang, K. Zhao, X. Xiao, and L. Zhang, "Synthesis and facet-dependent photoreactivity of BiOCl single-crystalline nanosheets," *Journal of the American Chemical Society*, vol. 134, no. 10, pp. 4473–4476, 2012.

[22] M. Guan, C. Xiao, J. Zhang et al., "Vacancy associates promoting solar-driven photocatalytic activity of ultrathin bismuth oxychloride nanosheets," *Journal of the American Chemical Society*, vol. 135, no. 28, pp. 10411–10417, 2013.

[23] J. Li, H. Li, G. Zhan, and L. Zhang, "Solar water splitting and nitrogen fixation with layered bismuth oxyhalides," *Accounts of Chemical Research*, vol. 50, no. 1, pp. 112–121, 2017.

[24] J. Li, Y. Yu, and L. Zhang, "Bismuth oxyhalide nanomaterials: layered structures meet photocatalysis," *Nanoscale*, vol. 6, no. 15, pp. 8473–8488, 2014.

[25] W. Ouyang, L. Su, and X. Fang, "UV photodetectors based on BiOCl nanosheet arrays: the effects of morphologies and electrode configurations," *Small*, vol. 14, no. 36, article 1801611, 2018.

[26] Y. Mi, L. Wen, Z. Wang et al., "Fe(III) modified BiOCl ultrathin nanosheet towards high-efficient visible- light photocatalyst," *Nano Energy*, vol. 30, pp. 109–117, 2016.

[27] W. Ouyang, F. Teng, and X. Fang, "High performance BiOCl nanosheets/TiO_2 nanotube arrays heterojunction UV photodetector: the influences of self-induced inner electric fields in the BiOCl nanosheets," *Advanced Functional Materials*, vol. 28, no. 16, article 1707178, 2018.

[28] W. Yang, Y. Wen, D. Zeng et al., "Interfacial charge transfer and enhanced photocatalytic performance for the heterojunction WO_3/BiOCl: first-principles study," *Journal of Materials Chemistry A*, vol. 2, no. 48, pp. 20770–20775, 2014.

[29] H. Wang, X. Yuan, Y. Wu et al., "Plasmonic Bi nanoparticles and BiOCl sheets as cocatalyst deposited on perovskite-type $ZnSn(OH)_6$ microparticle with facet- oriented polyhedron for improved visible-light-driven photocatalysis," *Applied Catalysis B: Environmental*, vol. 209, pp. 543–553, 2017.

[30] L. Sun, L. Xiang, X. Zhao et al., "Enhanced visible-light photocatalytic activity of BiOI/BiOCl heterojunctions: key role of crystal facet combination," *ACS Catalysis*, vol. 5, no. 6, pp. 3540–3551, 2015.

[31] Y. Wang, S. Sun, J. Zhang, Y. L. Huang, and W. Chen, "Recent progress in epitaxial growth of two-dimensional phosphorus," *SmartMat*, vol. 2, no. 3, pp. 286–298, 2021.

[32] X. Gao, Y. Zhu, D. Yi et al., "Ultrathin graphdiyne film on graphene through solution-phase van der Waals epitaxy," *Advances*, vol. 4, no. 7, article eaat6378, 2018.

[33] E. Shi, B. Yuan, S. B. Shiring et al., "Two-dimensional halide perovskite lateral epitaxial heterostructures," *Nature*, vol. 580, no. 7805, pp. 614–620, 2020.

[34] G. Peng, U. Tisch, O. Adams et al., "Diagnosing lung cancer in exhaled breath using gold nanoparticles," *Nature Nanotechnology*, vol. 4, no. 10, pp. 669–673, 2009.

[35] M. Struzik, I. Garbayo, R. Pfenninger, and J. L. Rupp, "A simple and fast electrochemical CO2Sensor based on Li7La3Zr2O12for environmental monitoring," *Advanced Materials*, vol. 30, no. 44, article 1804098, 2018.

[36] Y. Zou, X. Zhou, Y. Zhu, X. Cheng, D. Zhao, and Y. Deng, "sp^2-hybridized carbon-containing block copolymer templated synthesis of mesoporous semiconducting metal oxides with excellent gas sensing property," *Accounts of Chemical Research*, vol. 52, no. 3, pp. 714–725, 2019.

[37] S. Y. Jeong, J. S. Kim, and J. H. Lee, "Rational design of semiconductor-based chemiresistors and their libraries for next-generation artificial olfaction," *Advanced Materials*, vol. 32, no. 51, article 2002075, 2020.

[38] X. S. Wang, Z. W. Wang, J. D. Zhang et al., "Realization of vertical metal semiconductor heterostructures via solution phase epitaxy," *Nature Communications*, vol. 9, no. 1, article 3611, 2018.

[39] Z. Wang, Q. Jingjing, X. Wang et al., "Two-dimensional light-emitting materials: preparation, properties and applications," *Chemical Society Reviews*, vol. 47, no. 16, pp. 6128–6174, 2018.

[40] J. Dai, O. Ogbeide, N. Macadam et al., "Printed gas sensors," *Chemical Society Reviews*, vol. 49, no. 6, pp. 1756–1789, 2020.

[41] K. Yang, X. Wang, H. Li et al., "Composition- and phase-controlled synthesis and applications of alloyed phase

heterostructures of transition metal disulphides," *Nanoscale*, vol. 9, no. 16, pp. 5102–5109, 2017.

[42] Y. Zhang, F. Zhang, Y. Xu et al., "Epitaxial growth of topological insulators on semiconductors (Bi2Se3/Te@Se) toward high-performance photodetectors," *Methods*, vol. 3, no. 12, article 1900349, 2019.

[43] J. Yang, C. Wang, H. Ju et al., "Integrated quasiplane heteronanostructures of $MoSe_2/Bi_2Se_3$ hexagonal nanosheets: synergetic electrocatalytic water splitting and enhanced supercapacitor performance," *Advanced Functional Materials*, vol. 27, no. 48, article 1703864, 2017.

[44] J. Jin, Y. Wang, and T. He, "Preparation of thickness-tunable BiOCl nanosheets with high photocatalytic activity for photoreduction of CO_2," *RSC Advances*, vol. 5, no. 121, pp. 100244–100250, 2015.

[45] D. Wei, F. Tian, Z. Lu, H. Yang, and R. Chen, "Facile synthesis of Ag/AgCl/BiOCl ternary nanocomposites for photocatalytic inactivation of *S. aureus* under visible light," *RSC Advances*, vol. 6, no. 57, pp. 52264–52270, 2016.

[46] Y. Liu, D. Yao, L. Shen, H. Zhang, X. Zhang, and B. Yang, "Alkylthiol-enabled se powder dissolution in oleylamine at room temperature for the phosphine-free synthesis of copper-based quaternary selenide nanocrystals," *Journal of the American Chemical Society*, vol. 134, no. 17, pp. 7207–7210, 2012.

[47] H. Zhang, A. Alameen, X. An et al., "Theoretical and experimental investigations of BiOCl for electrochemical adsorption of cesium ions," *Physical Chemistry Chemical Physics*, vol. 21, no. 37, pp. 20901–20908, 2019.

[48] X. Zhang, G. Li, C. Fan, G. Ding, Y. Wang, and P. Han, "Theoretical insights into the adsorption of monatomic Ag on the (2×2) BiOCl (0 0 1) surfaces," *Computational Materials Science*, vol. 95, pp. 113–120, 2014.

[49] G. B. Osterhoudt, R. Carelli, K. S. Burch, F. Katmis, N. Gedik, and J. S. Moodera, "Charge transfer inEuS/Bi2Se3heterostructures as indicated by the absence of Raman scattering," *Physical Review B*, vol. 98, no. 1, article 014308, 2018.

[50] S. Bhattacharyya, G. Akhgar, M. Gebert, J. Karel, M. T. Edmonds, and M. S. Fuhrer, "Recent progress in proximity coupling of magnetism to topological insulators," *Advanced Materials*, vol. 33, no. 33, article 2007795, 2021.

[51] Z. Wu, L. Rong, J. Yang et al., "Ion-conductive hydrogel-based stretchable, self-healing, and transparent NO_2 sensor with high sensitivity and selectivity at room temperature," *Small*, vol. 17, no. 52, article 2104997, 2021.

[52] D. Feuerstein, K. H. Parker, and M. G. Boutelle, "Practical methods for noise removal: applications to spikes, nonstationary quasi-periodic noise, and baseline drift," *Analytical Chemistry*, vol. 81, no. 12, pp. 4987–4994, 2009.

[53] C. H. Park, V. Schroeder, B. J. Kim, and T. M. Swager, "Ionic liquid-carbon nanotube sensor arrays for human breath related volatile organic compounds," *ACS Sensors*, vol. 3, no. 11, pp. 2432–2437, 2018.

[54] E. Wu, Y. Xie, B. Yuan et al., "Ultrasensitive and fully reversible NO2Gas sensing based on p-type MoTe2under ultraviolet illumination," *ACS Sensors*, vol. 3, no. 9, pp. 1719–1726, 2018.

[55] J. Wang, E. Fatima-Ezzahra, J. Dai et al., "Ligand-assisted deposition of ultra-small Au nanodots on Fe_2O_3/reduced graphene oxide for flexible gas sensors," *Nanoscale Advances*, vol. 4, no. 5, pp. 1345–1350, 2022.

[56] S. Li, Z. Wang, X. Wang et al., "Orientation controlled preparation of nanoporous carbon nitride fibers and related composite for gas sensing under ambient conditions," *Nano Research*, vol. 10, no. 5, pp. 1710–1719, 2017.

[57] J. Bao, S. Zeng, J. Dai et al., "Heterostructures between a tin-based intermetallic compound and a layered semiconductor for gas sensing," *Chemical Communications*, vol. 57, no. 45, pp. 5590–5593, 2021.

[58] L. Zhao, N. Guanhua, S. Lulu et al., "Effect of ionic liquid treatment on pore structure and fractal characteristics of low rank coal," *Fuel*, vol. 262, article 116513, 2020.

[59] Q. Yu, J. Zhu, Z. Xu, and X. Huang, "Facile synthesis of α-Fe_2O_3@SnO_2 core-shell heterostructure nanotubes for high performance gas sensors," *Sensors and Actuators B: Chemical*, vol. 213, pp. 27–34, 2015.

[60] J.-S. Kim, H.-W. Yoo, H. O. Choi, and H.-T. Jung, "Tunable volatile organic compounds sensor by using thiolated ligand conjugation on MoS_2," *Nano Letters*, vol. 14, no. 10, pp. 5941–5947, 2014.

[61] D. Ju, H. Xu, Z. Qiu, J. Guo, J. Zhang, and B. Cao, "Highly sensitive and selective triethylamine-sensing properties of nanosheets directly grown on ceramic tube by forming NiO/ZnO PN heterojunction," *Sensors and Actuators B: Chemical*, vol. 200, pp. 288–296, 2014.

[62] B. Sharma, A. Sharma, and J.-H. Myung, "Selective ppb-level NO_2 gas sensor based on SnO_2-boron nitride nanotubes," *Sensors and Actuators B: Chemical*, vol. 331, article 129464, 2021.

[63] W. Zheng, Y. Xu, L. Zheng et al., "MoS2 Van der Waals p–n junctions enabling highly selective room-temperature NO2 sensor," *Advanced Functional Materials*, vol. 30, no. 19, article 2000435, 2020.

[64] J. Cao, Q. Chen, X. Wang et al., "Recent development of gas sensing platforms based on 2D atomic crystals," *Research*, vol. 2021, article 9863038, 2021.

[65] G. Cui, M. Zhang, and G. Zou, "Resonant tunneling modulation in quasi-2D Cu_2O/SnO_2 p-n horizontal-multilayer heterostructure for room temperature H_2S sensor application," *Scientific Reports*, vol. 3, no. 1, article 1250, 2013.

[66] L. Jiang, K. Xue, Z. Chen, Q. Cui, and S. Xu, "High performance of gas sensor based on Bi-doped $ZnSnO_3$/CuO nanocomposites for acetone," *Microporous and Mesoporous Materials*, vol. 329, article 111532, 2022.

[67] Y. Hu, J. Zhou, P.-H. Yeh, Z. Li, T. Y. Wei, and Z. L. Wang, "Supersensitive, fast-response nanowire sensors by using Schottky contacts," *Advanced Materials*, vol. 22, no. 30, pp. 3327–3332, 2010.

[68] J. Choi, Y.-J. Kim, S.-Y. Cho et al., "In situ formation of multiple Schottky barriers in a Ti_3C_2 MXene film and its application in highly sensitive gas sensors," *Advanced Functional Materials*, vol. 30, no. 40, article 2003998, 2020.

[69] H. J. Park, W.-J. Kim, H.-K. Lee et al., "Highly flexible, mechanically stable, and sensitive NO_2 gas sensors based on reduced graphene oxide nanofibrous mesh fabric for flexible electronics," *Sensors and Actuators B: Chemical*, vol. 257, pp. 846–852, 2018.

[70] P.-G. Su and H.-C. Shieh, "Flexible NO_2 sensors fabricated by layer-by-layer covalent anchoring and in situ reduction of graphene oxide," *Sensors and Actuators B: Chemical*, vol. 190, pp. 865–872, 2014.

[71] J. Wu, Z. Wu, H. Ding et al., "Flexible, 3D SnS_2/reduced graphene oxide heterostructured NO_2 sensor," *Sensors and Actuators B: Chemical*, vol. 305, article 127445, 2020.

[72] Z. Yang, L. Jiang, J. Wang et al., "Flexible resistive NO_2 gas sensor of three-dimensional crumpled MXene $Ti_3C_2T_x$/ZnO spheres for room temperature application," *Sensors and Actuators B: Chemical*, vol. 326, article 128828, 2021.

[73] U. Yaqoob, A. S. M. I. Uddin, and G.-S. Chung, "A high-performance flexible NO_2 sensor based on WO_3 NPs decorated on MWCNTs and RGO hybrids on PI/PET substrates," *Sensors and Actuators B: Chemical*, vol. 224, pp. 738–746, 2016.

[74] H. Liu, M. Li, O. Voznyy et al., "Physically flexible, rapid-response gas sensor based on colloidal quantum dot solids," *Advanced Materials*, vol. 26, no. 17, pp. 2718–2724, 2014.

[75] J. Wu, Z. Wu, H. Ding et al., "Three-dimensional graphene hydrogel decorated with SnO2 for high-performance NO2 sensing with enhanced immunity to humidity," *ACS Applied Materials & Interfaces*, vol. 12, no. 2, pp. 2634–2643, 2020.